INTERNATIONAL JOURNAL FOR NUMERICAL METHODS IN FLUIDS
Int. J. Numer. Meth. Fluids 2010; **62**:765–783
Published online 24 March 2009 in Wiley InterScience (www.interscience.wiley.com). DOI: 10.1002/fld.2043

Simulating 3D deformable particle suspensions using lattice Boltzmann method with discrete external boundary force

Jingshu Wu and Cyrus K. Aidun*, †

G. W. Woodruff School of Mechanical Engineering, Georgia Institute of Technology, 500 10th Street NW, Atlanta, GA 30332, U.S.A.

SUMMARY

A method for direct numerical analysis of three-dimensional deformable particles suspended in fluid is presented. The flow is computed on a fixed regular 'lattice' using the lattice Boltzmann method (LBM), where each solid particle is mapped onto a Lagrangian frame moving continuously through the domain. Instead of the bounce-back method, an external boundary force (EBF) is used to impose the no-slip boundary condition at the fluid–solid interface for stationary or moving boundaries. The EBF is added directly to the lattice Boltzmann equation. The motion and orientation of the particles are obtained from Newtonian dynamics equations. The advantage of this approach is outlined in comparison with the standard and higher-order interpolated bounce-back methods as well as the LBM immersed-boundary and the volume-of-fluid methods. Although the EBF method is general, in this application, it is used in conjunction with the lattice–spring model for deformable particles. The methodology is validated by comparing with experimental and theoretical results. Copyright © 2009 John Wiley & Sons, Ltd.

Received 7 October 2008; Revised 9 February 2009; Accepted 10 February 2009

KEY WORDS: lattice Boltzmann; bounce back; fluid solid interaction; external boundary force; no-slip condition; lattice spring; red blood cell

1. INTRODUCTION

The lattice Boltzmann method (LBM) for the analysis of fluid flow problems [1–3] has been extended to direct simulation of particles suspended in fluid [4–6]. In these methods, the no-slip boundary condition at the fluid–solid interface is based on the standard 'bounce-back' (SBB) rule. The interaction boundary is represented at the midpoints of the links, which are cut by the solid particle boundary. A fluid–solid collision function is used to account for the momentum exchange

*Correspondence to: Cyrus K. Aidun, G. W. Woodruff School of Mechanical Engineering, Georgia Institute of Technology, 500 10th Street NW, Atlanta, GA 30332, U.S.A.
†E-mail: cyrus.aidun@me.gatech.edu

Contract/grant sponsor: Publishing Arts Research Council; contract/grant number: 98-1846389

and apply the interaction force to both fluid and the particle. In the earlier method presented by Ladd [6], the lattice nodes on either side of the boundary are treated identically allowing the fluid to fill the whole domain both inside and outside the 'solid' particle. The effect of the interior fluid on the dynamics of the solid particle is discussed by Ladd [6]. In an alternative method presented by Aidun and Lu [4] and Aidun *et al.* [5], there are no fluid nodes inside the solid particle. However, both of these approaches use the transfer of population density in the LB equation to account for the momentum transfer at the fluid–solid interface.

The SBB method has been used for the simulation of deformable particles with some success. Buxton *et al.* [7] combine the LBM with lattice–spring model (LSM) to study the interaction and deformation of an elastic shell with the surrounding fluid. Dupin *et al.* [8] use a two-dimensional (2D) spring mesh to model the elastic membrane. MacMeccan *et al.* [9] use a combination of the LBM for the fluid and finite element method (FEM) for the solid domain to simulate 800 deformable red blood cells (RBCs) at 45% concentration. All of these studies use the SBB boundary conditions as it is easy to implement in 3D deformable particle simulations. However, with SBB the solid boundary (broken line in Figure 1(a)) will not move continuously and smoothly in space; instead it will jump from one midpoint to another causing fluctuations. To reduce this fluctuation, one can use a finer lattice grid with more nodes at the boundary increasing the computational time or higher-order bounce back based on interpolations. Recently, the bounce-back scheme has been improved by using spatial linear, quadratic, and multi-reflection interpolations [10–12]. Although the interpolated bounce-back (IBB) methods are more accurate, in addition, to being computationally expensive, they require at least two or three fluid nodes between nearby solid surfaces for interpolation. This excludes the application to non-dilute suspensions of solid particles with close interaction between the particles or the particle and the boundary [13, 14].

A modified approach analogous to the volume-of-fluid method has been developed [15–17] based on a modified collision operator for the fluid nodes that are partially covered by solid. The

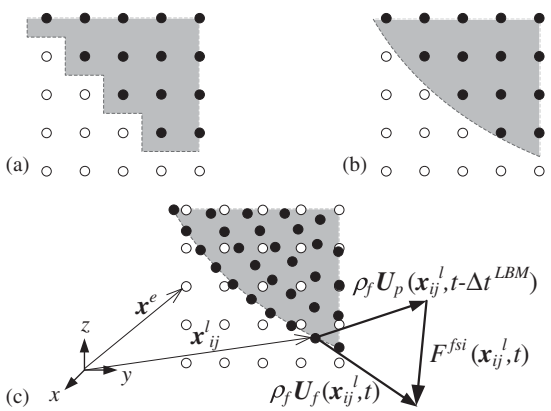

Figure 1. (a) Regular Eulerian grid for standard bounce-back (SBB) rule; (b) regular Eulerian grid for interpolated bounce-back (IBB) rule. In (a) the filled circles (•) are the fluid nodes covered by the solid and open circles (○) are the fluid nodes outside the solid particle; (c) the solid Lagrangian nodes (•) and fluid Eulerian nodes (○) for external boundary force (EBF) method. The broken line (···) shows the solid boundary. Note that the solid boundary nodes in the (c) are located exactly on the fluid–solid boundary Γ.

DOI: 10.1002/fld

fluid lattices covered by the particle have the same velocity as the solid particle. The collision operator for fluid lattices partially covered by the particle is modified so that the collision force in each discrete direction is the product of the local moment difference between the fluid and solid in that direction. The solid fraction coefficient varies between 0 for completely fluid filled nodes and 1 for the nodes completely covered by solid. This method requires accurate account of the solid fraction at each time step in every fluid lattice. Otherwise, the computations may cause fluctuation in velocity and force when the particle boundary crosses a fluid node. This approach could become tedious as it is difficult to calculate the solid volume fraction accurately for 3D simulations with irregular or deformable solid particle.

Another way to solve fluid–solid interaction is the immersed-boundary method (IBM), which uses two grid systems and assumes that the solid boundary nodes are connected by a set of high stiffness springs. This method, introduced by Peskin [18], has been applied to LBM [19] for simulation of solid particle suspension. The basic steps in IBM are to (1) move each immersed solid point based on the velocity obtained by interpolating the surrounding fluid velocity, (2) calculate the internal elastic forces generated by the deformation of the boundary, (3) distribute the internal elastic forces to the fluid by the same interpolating function from step 1, and (4) solve the discrete form of the Navier–Stokes equations by using this force as the driving force to obtain the new fluid velocity field. Recently, Zhang *et al.* [20] extended this approach to simulation deformable 2D capsules. In this scheme, the fluid–solid interaction force is based on the internal elastic force as the membrane deforms and moves with local fluid velocity. The IBM is very effective as used in conjunction with the LBM. However, it requires an artificial penalty parameter representing the high stiffness spring constant for the links connecting the boundary nodes of the rigid or stiff solid particles. In addition, the fluid–solid interaction force is based on the internal spring force generated by the small deformation of the solid boundary with high stiffness. This can cause instability problems in the analysis of suspended particles or capsules with deformable membrane.

In this paper, we implement a no-slip boundary condition in the LBM for stationary and moving solid particles based on the EBF approach developed for the Navier–Stokes equation by Goldstein *et al.* [21]. With the discrete EBF, we consider two overlapping grid systems; a regular Eulerian grid for the fluid domain and a Lagrangian grid for the solid domain. The no-slip boundary condition at the solid surface is applied by adding a force density to the fluid domain to force the difference between the fluid and the solid velocity at the boundary nodes to be zero; and the counterforce acting on the solid particles to update the position and velocity of the particles based on Newtonian dynamics equations. The lattice Boltzmann equation with the additional boundary force density in the form of a source term is solved to obtain the updated fluid velocity. We show that this approach results in smoother fluid–solid interaction force as compared with SBB, and in general, more stable as compared with the LBM with SBB or IBM (with deformable particles). For example, coupling the LBM with the LSM could cause instabilities when increasing the spring constant or reducing $\Delta x^{\mathrm{LSM}}/\Delta x^{\mathrm{LBM}}$, the ratio between the unit grid size of LSM and LBM [7, 22]. To reduce this instability in LBM with SBB or IBM, one has to either increase the size of the particle (the solid grid size) or use a finer fluid grid to increase the number of boundary nodes—both approaches will increase the computational cost. We show that the EBF approach presented here reduces this instability.

The presence of an external *body* force in the kinetic-based conservation equations has been discussed in classical kinetic theory [23]. The connection between the source term in the LBE and the resulting *body* force field in the Navier–Stokes equation has also been discussed since the inception of the LBM two decades ago [24–28]. A method based on an EBF at the

DOI: 10.1002/fld

fluid–solid interface of the moving particle in the Navier–Stokes equation at the fluid–solid boundary [21] to implement the no-slip boundary condition in the LBM for simulation of solid particles and deformable capsules with a simple algorithm and no tunable parameters is presented here.

The remaining part of this paper is organized as follows. In Section 2, the EBF method is described in detail covering the basics of the fluid–solid interaction including a summary of the basic steps. Several sample simulations with rigid solid particles are presented and compared with theoretical solutions and experimental results in Section 3 to validate the accuracy of the method. Results for single and large numbers of 3D capsules with deformable membrane (RBCs) are presented in Section 4 including comparison with experimental data. The advantages and the limitations of the method are discussed in Section 5.

2. METHODOLOGY

2.1. Fluid–solid interaction

Fluid flow over a solid particle results in normal and shear forces exerted by the fluid on the particle and, conversely, by the particle on the fluid, referred to as the fluid–solid interaction force. This forces the fluid adjacent to the solid surface to move with the surface velocity (no-slip). If an EBF identical to the fluid–solid interaction force is exerted on the fluid, the fluid will move with the same velocity. In other words, the effect of the particle motion on the fluid motion could be identically replaced by an EBF [21]. Let Π_s and Π_f represent the continuum solid and fluid domains, separated by the solid–fluid boundary, Γ. Here, subscripts s and f serve to symbolically distinguish the solid and fluid domains, respectively. The set of position vectors of the solid and fluid nodes are represented by Π_s^N and Π_f^M, where superscripts N and M denote the solid nodes and fluid nodes, respectively. The subsets for solid and fluid boundary nodes are represented by Γ_s and Γ_f, respectively. Note that because with this method, the solid boundary nodes are exactly on the solid boundary, one can consider Γ_s as a subset of Γ. We use $\mathbf{x}$ with components (x, y, z) as the position vector in the fixed Cartesian coordinate system. As shown in Figure 1(c), the position vector for the jth node on ith particle is given by $\mathbf{x}_{ij}^{\mathrm{l}} \in \Pi_s^N$, the position vector for the fluid nodes is represented by $\mathbf{x}^{\mathrm{e}} \in \Pi_f^M$, where superscripts l and e serve to symbolically distinguish the position vector for solid nodes and fluid nodes, respectively. Let $\mathbf{F}^{\mathrm{fsi}}(\mathbf{x}, t)$ and $\mathbf{g}(\mathbf{x}, t)$ represent the force per unit volume acting, respectively, on the solid and the fluid points $\mathbf{x}$ on Γ at time, t. Therefore, $\mathbf{F}^{\mathrm{fsi}}(\mathbf{x}, t) = -\mathbf{g}(\mathbf{x}, t)$ for $\mathbf{x} \in \Gamma$. However, the force on the fluid boundary node $\mathbf{x}^{\mathrm{e}}$ is given by $\mathbf{g}(\mathbf{x}^{\mathrm{e}}, t)$ which is not equal to $\mathbf{F}^{\mathrm{fsi}}(\mathbf{x}, t)$ when $\mathbf{x} \in \Gamma$. The Navier–Stokes and continuity equations with the EBF can be written as

$$\rho\left(\frac{\partial \mathbf{u}}{\partial t} + \mathbf{u}\cdot\nabla\mathbf{u}\right) = -\nabla p + \mu\nabla^2\mathbf{u} + \mathbf{g}(\mathbf{x}, t)$$
$$\nabla\cdot\mathbf{u} = 0 \tag{1}$$

where $\mathbf{x} \in \Pi_f$, and in this equation, $\mathbf{g}(\mathbf{x}, t) = 0$ when $\mathbf{x} \notin \Gamma$. In the discretized formulation, the EBF, $\mathbf{g}$, is evaluated on the fluid boundary node by interpolation to find $\mathbf{g}(\mathbf{x}^{\mathrm{e}}, t)$, as shown below (see Equation (6)).

DOI: 10.1002/fld

In most situations, the boundary nodes will not coincide with the fluid nodes, so the fluid velocity defined by $\mathbf{U}_{\mathrm{f}}(\mathbf{x}_{ij}^{\mathrm{l}},t)$ at solid boundary node $\mathbf{x}_{ij}^{\mathrm{l}}$ at time t should be interpolated by

$$\mathbf{U}_{\mathrm{f}}(\mathbf{x}_{ij}^{\mathrm{l}},t)=\int_{\Pi_{\mathrm{f}}^{M}}\mathbf{u}(\mathbf{x}^{\mathrm{e}},t)D(\mathbf{x}^{\mathrm{e}}-\mathbf{x}_{ij}^{\mathrm{l}})\,\mathrm{d}\mathbf{x}^{\mathrm{e}},\quad \mathbf{x}_{ij}^{\mathrm{l}}\in\Gamma_{\mathrm{s}} \tag{2}$$

where $D(\mathbf{x}^{\mathrm{e}}-\mathbf{x}_{ij}^{\mathrm{l}})$ is a discrete Dirac delta function in 3D domain [29],

$$D(\mathbf{x})\equiv\begin{cases}\dfrac{1}{64h^3}\left(1+\cos\left(\dfrac{\pi x}{2h}\right)\right)\left(1+\cos\left(\dfrac{\pi y}{2h}\right)\right)\left(1+\cos\left(\dfrac{\pi z}{2h}\right)\right) & \text{if } |\mathbf{x}|\leqslant 2h\\ 0 & \text{otherwise}\end{cases} \tag{3}$$

where $h\equiv\Delta x^{\mathrm{LBM}}$ is the unit lattice length in LBM calculation. For linear velocity distributions, the interpolation (3) can give exact solution. For smooth velocity distributions (continuous first-order derivative), the interpolation has second-order accuracy. However, the velocity profile at the boundary is usually not smooth and, subsequently, relation (2) is only first-order accurate at the boundary. Further improvement to achieve higher-order accuracy is under investigation.

The initial velocity in the fluid domain and the particle position and velocity are known. The fluid velocity at the particle boundary is equal to the particle velocity due to no-slip condition, therefore,

$$\mathbf{U}_{\mathrm{f}}(\mathbf{x}_{ij}^{\mathrm{l}},t-\Delta t^{\mathrm{LBM}})=\mathbf{U}_{p}(\mathbf{x}_{ij}^{\mathrm{l}},t-\Delta t^{\mathrm{LBM}}) \tag{4}$$

where the LBM time step $\Delta t^{\mathrm{LBM}}=1$, the term $\mathbf{U}_{p}(\mathbf{x}_{ij}^{\mathrm{l}},t-\Delta t^{\mathrm{LBM}})$ is the particle velocity at solid boundary node $\mathbf{x}_{ij}^{\mathrm{l}}$ at the previous time step. The fluid–solid interaction force $\mathbf{F}^{\mathrm{fsi}}(\mathbf{x}_{ij}^{\mathrm{l}},t)$ acting on the solid particle boundary node is given by

$$\mathbf{F}^{\mathrm{fsi}}(\mathbf{x}_{ij}^{\mathrm{l}},t)=\rho_{f}(\mathbf{U}_{\mathrm{f}}(\mathbf{x}_{ij}^{\mathrm{l}},t)-\mathbf{U}_{p}(\mathbf{x}_{ij}^{\mathrm{l}},t-\Delta t^{\mathrm{LBM}}))/\Delta t^{\mathrm{LBM}},\quad \mathbf{x}_{ij}^{\mathrm{l}}\in\Gamma_{\mathrm{s}} \tag{5}$$

where ρ_{f} is the density of the fluid. The resulting force acting on the fluid boundary nodes is given by

$$\mathbf{g}(\mathbf{x}^{\mathrm{e}},t)=-\int_{\Gamma_{\mathrm{s}}}\mathbf{F}^{\mathrm{fsi}}(\mathbf{x}_{ij}^{\mathrm{l}},t)D(\mathbf{x}^{\mathrm{e}}-\mathbf{x}_{ij}^{\mathrm{l}})\,\mathrm{d}\mathbf{x}_{ij}^{\mathrm{l}},\quad \mathbf{x}^{\mathrm{e}}\in\Gamma_{\mathrm{f}} \tag{6}$$

where $\mathbf{g}$ will be used as an EBF term in the LB equation as will be discussed in Section 2.2.

$\mathbf{F}(\mathbf{x}_{ij}^{\mathrm{l}},t)$ is the combination of the fluid–solid interaction force $\mathbf{F}^{\mathrm{fsi}}(\mathbf{x}_{ij}^{\mathrm{l}},t)$ and the external force $\mathbf{F}^{\mathrm{ext}}(\mathbf{x}_{ij}^{\mathrm{l}},t)$ which could include the gravitational force, interparticle (electrical or lubrication) forces; therefore,

$$\mathbf{F}(\mathbf{x}_{ij}^{\mathrm{l}},t)=\mathbf{F}^{\mathrm{fsi}}(\mathbf{x}_{ij}^{\mathrm{l}},t)+\mathbf{F}^{\mathrm{ext}}(\mathbf{x}_{ij}^{\mathrm{l}},t),\quad \mathbf{x}_{ij}^{\mathrm{l}}\in\Gamma_{\mathrm{s}} \tag{7}$$

So for the ith particle with N boundary nodes, if we assume the center of gravity of the particle is $\mathbf{x}_{i}^{\mathrm{lc}}$, then the total force $\mathbf{F}_{i}$ and the torque $\mathbf{T}_{i}$ on this particle are given by

$$\mathbf{F}_{i}(t)=\sum_{j=1}^{N}\mathbf{F}(\mathbf{x}_{ij}^{\mathrm{l}},t) \tag{8}$$

DOI: 10.1002/fld

and

$$\mathbf{T}_i(t) = \sum_{j=1}^{N} (\mathbf{x}_{ij}^{\mathrm{l}} - \mathbf{x}_i^{lc}) \times \mathbf{F}(\mathbf{x}_{ij}^{\mathrm{l}}, t) \tag{9}$$

respectively.

The Newtonian dynamics equations for the ith particle are given by

$$\begin{aligned} M_i \frac{\mathrm{d}\mathbf{U}_i}{\mathrm{d}t} &= \mathbf{F}_i \\ \mathbf{I}_i \frac{\mathrm{d}\boldsymbol{\Omega}_i}{\mathrm{d}t} + \boldsymbol{\Omega}_i \times (\mathbf{I}_i \cdot \boldsymbol{\Omega}_i) &= \mathbf{T}_i \end{aligned} \tag{10}$$

where M_i and $\mathbf{I}_i$ are the mass and the inertial tensor of the ith particle; and the velocity, $\mathbf{U}_i$, and angular velocity, $\boldsymbol{\Omega}_i$, can be computed by numerical solution of Equation (10). Note that in Equation (10), the term $\mathrm{d}\boldsymbol{\Omega}_i/\mathrm{d}t$ is dependent on $\boldsymbol{\Omega}_i$, so a simple Euler integration may not give accurate results. A fourth-order accurate Runge–Kutta integration procedure is being used in this study.

2.2. LBM with EBF

The LBM uses a regular Eulerian grid in the fluid domain. The fluid is modeled as a group of fluid particles moving with discrete velocity. The state of the fluid at node $\mathbf{x}^{\mathrm{e}}$ at time t is described by the distribution function, $f_k(\mathbf{x}^{\mathrm{e}}, t)$, which is calculated by the lattice Boltzmann equation [1–3, 5]

$$f_k(\mathbf{x}^{\mathrm{e}} + \mathbf{e}_k, t+1) = f_k(\mathbf{x}^{\mathrm{e}}, t) + \frac{1}{\tau}[f_k^{\mathrm{eq}}(\mathbf{x}^{\mathrm{e}}, t) - f_k(\mathbf{x}^{\mathrm{e}}, t)] \tag{11}$$

Here, $f_k^{\mathrm{eq}}(\mathbf{x}^{\mathrm{e}}, t)$ is the equilibrium distribution function at $(\mathbf{x}^{\mathrm{e}}, t)$, τ is the single relaxation time constant and $\mathbf{e}_k$ is the discrete velocity vector. The fluid density ρ and the macroscopic fluid velocity $\mathbf{u}(\mathbf{x}^{\mathrm{e}}, t)$ are obtained from the first two moments, given by

$$\rho(\mathbf{x}^{\mathrm{e}}, t) = \sum_k f_k(\mathbf{x}^{\mathrm{e}}, t) \quad \text{and} \quad \rho(\mathbf{x}^{\mathrm{e}}, t)\mathbf{u}(\mathbf{x}^{\mathrm{e}}, t) = \sum_k f_k(\mathbf{x}^{\mathrm{e}}, t)\mathbf{e}_k \tag{12}$$

The most common lattice model for 2D case is D2Q9 model, which uses nine discrete velocity directions, while the model for 3D case is D3Q19, which uses cubic lattice with 19 discrete velocity directions [5] for the fluid particles moving along the horizontal, vertical, and diagonal links. The equilibrium distribution function is defined as

$$f_k^{\mathrm{eq}} = w_k \rho[1 + 3\mathbf{e}_k \cdot \mathbf{u} + \tfrac{9}{2}(\mathbf{e}_k \cdot \mathbf{u})^2 - \tfrac{3}{2}\mathbf{u}^2] \tag{13}$$

with $w_0 = \frac{4}{9}$ for fluid particles at rest, $w_{1-4} = \frac{1}{9}$ for fluid particles moving in the non-diagonal directions, and $w_{5-8} = \frac{1}{36}$ for the diagonal directions in 2D D2Q9 model; and $w_0 = \frac{1}{3}$, $w_{1-6} = \frac{1}{18}$ (non-diagonal directions), and $w_{7-18} = \frac{1}{36}$ (diagonal directions) in 3D D3Q19 model. For the present model, the pseudospeed of sound is $c_{\mathrm{s}} = \sqrt{1/3}$ and the kinematic viscosity is $\nu = (2\tau - 1)/6$. In the longer time scale, the LBM is effectively solving the Navier–Stokes equations [30–32].

The lattice Boltzmann operators must be modified at the boundary to fit the wall boundary conditions. In this paper, three different wall boundary conditions are applied. These are the

DOI: 10.1002/fld

periodic, no-slip wall, and the stress-free conditions. Details about these boundary conditions can be found in an earlier publication [5, 14].

To simulate the interactions between the fluid and the solid particles, the LBM with bounce back must incorporate the boundary conditions imposed on the fluid by the solid particles. In the conventional LBM, fluid and solid domains share one regular Eulerian grid (Figure 1(a), (b)). The nodes are scanned at each time step to mark the fluid nodes outside the solid and the fluid nodes inside the solid boundary. The interaction is calculated by the lattice links that connect the inside and outside fluid nodes. This operation is relatively computationally expensive.

The EBF method presented here involves two independent but overlapping grid systems. The Eulerian grid represents the fluid domain where each particle is modeled with a Lagrangian grid. The suspended particles move continuously in space while the no-slip boundary condition on the surface of the particle is satisfied by the requirement that the fluid velocity at the solid boundary node is equal to the solid velocity at that point. We have to emphasize here that the solid boundary in LBM with SBB and the LBM with EBF is different—in SBB it is halfway between fluid and solid nodes, where in EBF the solid boundary represented by the Lagrangian grid nodes is the actual and the precise boundary of the particle moving continuously through the fluid domain, as show in Figure 1(c).

The lattice Boltzmann equation should be modified to include the fluid–solid interaction force $\mathbf{g}$ from Equation (6) by adding an additional term to the collision function. This changes the lattice Boltzmann equation to

$$f_k(\mathbf{x}^e+\mathbf{e}_k, t+1) = f_k(\mathbf{x}^e, t) + \frac{1}{\tau}[f_k^{eq}(\mathbf{x}^e, t) - f_k(\mathbf{x}^e, t)] + \frac{3}{2} w_k \mathbf{g}\cdot\mathbf{e}_k \tag{14}$$

Although a similar term is also used in the IBM by Feng and Michaelides [19], the method for calculating the fluid–solid interaction force is very different. With the EBF method, $\mathbf{g}$ is computed from (6) by the velocity difference between fluid and solid at the boundary nodes, whereas in IBM, the interaction force is the internal spring force generated by the small deformation of the solid boundary with high solid stiffness. In addition, the way to calculate the dynamics of the solid particle is different. We integrate Equation (10) to capture the motion of the solid particle, whereas in IBM the solid nodes move with the local fluid velocity.

2.3. Extension to deformable particles

Various numerical schemes can be applied for computation of the particle deformation. For example, the FEM has been coupled to the LB equations to simulate suspension of deformable particles [9]. Here, we simulate the particle deformation using the LSM. This method consists of a set of Hookean lattice–spring links connecting regularly spaced mass nodes. It has been shown that the large-scale behavior of the LSM system can be mapped onto continuum elasticity theory [22]. In this method, the elastic links that generate the stretching energy act as Hooke's Law springs. For small deformations, the elastic energy associated with the ith node is

$$E_i = \frac{k}{2}\sum_{j=1}^{n}(|\mathbf{r}_{ij}| - |\mathbf{r}_{ij}^{eq}|)^2 \tag{15}$$

Here, k is the spring constant, n is the total number of nodes that connect with node i, $|\mathbf{r}_{ij}|$ is the length between the node i and j, $|\mathbf{r}_{ij}^{eq}|$ is the force-free equilibrium spring length between

DOI: 10.1002/fld

i and j. The elastic force $\mathbf{F}_{ij}^{\mathrm{s}}$ acting on the lattice node i due to node j is calculated from the derivative of the energy function

$$\mathbf{F}_{ij}^{\mathrm{s}} = -\frac{\partial E_i}{\partial \mathbf{r}_{ij}} = -k\left(\frac{|\mathbf{r}_{ij}| - |\mathbf{r}_{ij}^{\mathrm{eq}}|}{|\mathbf{r}_{ij}|}\right)\mathbf{r}_{ij} \tag{16}$$

So the total spring force acting on node i is

$$\mathbf{F}_i^{\mathrm{s}T} = \sum_{j=1}^{n} \mathbf{F}_{ij}^{\mathrm{s}} \tag{17}$$

This internal solid force is generated by the extension or contraction of the spring links. For small deformations, this simple model is proved to follow the linear elasticity theory with Young's modulus $E = 5k/2\Delta x^{\mathrm{LSM}}$, Poisson's ratio $v = \frac{1}{4}$ and the speed of sound $c_{\mathrm{s}} = \Delta x^{\mathrm{LSM}}\sqrt{3k/m_i}$ [22]. Here, Δx^{LSM} is the unit link length of the lattice spring and m_i is the mass assigned to each node. One can change Poisson's ratio by introducing the harmonic potential, rotational potential, or additional multi-body interaction terms in the energy function and elastic force function of LSM [33, 34].

There are two basic approaches to calculate the deformation of the solid by using LSM as outlined below. One way is to use an explicit scheme where mass is assigned on each node based on the solid density and the total force acting on the ith node is given by

$$\mathbf{F}_i^{\mathrm{tot}} = \mathbf{F}_i^{\mathrm{s}T} + \mathbf{F}_i^{\mathrm{fsi}} + \mathbf{F}_i^{\mathrm{ext}} \tag{18}$$

Here, $\mathbf{F}_i^{\mathrm{s}T}$ is the spring force, $\mathbf{F}_i^{\mathrm{fsi}}$ is the fluid–solid interaction force and $\mathbf{F}_i^{\mathrm{ext}}$ is the external force. Then we integrate Newton's equation of motion, $\mathbf{F}_i^{\mathrm{tot}} = m_i(\partial^2 \mathbf{r}_i/\partial t^2)$, with an explicit method to update the acceleration, velocity, and the position for every LS nodes. This method is straightforward and easy to implement, but it has to meet certain stability requirements [35]. The Courant number $Cr = c_{\mathrm{s}}\Delta t/\Delta x^{\mathrm{LSM}}$ needs to be smaller than one to reduce the fluctuations in the fluid–solid interaction force, and $\Delta x^{\mathrm{LSM}} \geqslant \Delta x^{\mathrm{LBM}}$. These conditions impose a severe limitation on the applicability of this method. In 3D calculations, in order to reduce the computation cost, it is usually preferred to have $\Delta x^{\mathrm{LSM}} < \Delta x^{\mathrm{LBM}}$.

The second approach is to use an implicit scheme where at each time step the particle will first move without deformation due to $\mathbf{F}_i^{\mathrm{fsi}} + \mathbf{F}_i^{\mathrm{ext}}$, then under the same force, the particle will deform. Each lattice–spring node will instantly relax to its equilibrium state, the spring force $\mathbf{F}_i^{\mathrm{s}T}$ at each solid node is given by $\mathbf{F}_i^{\mathrm{s}} = -(\mathbf{F}_i^{\mathrm{fsi}} + \mathbf{F}_i^{\mathrm{ext}})$, and based on Equation (16), we can write

$$\mathbf{r}_i = \frac{1}{n}\left[\frac{\mathbf{F}_i^{\mathrm{fsi}} + \mathbf{F}_i^{\mathrm{ext}}}{k} + \sum_{j=1, j\neq i}^{n}\left(\frac{|\mathbf{r}_{ij}^{\mathrm{eq}}|}{|\mathbf{r}_{ij}|}\mathbf{r}_{ij} + \mathbf{r}_j\right)\right] \tag{19}$$

The implicit method is more stable than the explicit method, although it may require additional computational time in the deformation calculations. However, considering that the lattice–spring deformation calculations are a small part of the whole simulation, especially in the simulations that have large number of deformable particles with particle–particle interaction, the implicit scheme seems to be a better choice.

DOI: 10.1002/fld

The computational algorithm that has been used in the EBF LB–LSM method can be summarized as follows:

(i) At $t=t_0$, the initial fluid velocity in the fluid domain and the particle velocity/position are known.
(ii) The fluid velocity $\mathbf{U}_f$ on the boundary node is obtained by Equation (2), the fluid–solid interaction force $\mathbf{F}^{fsi}$ from Equation (5) is applied on the solid boundary nodes.
(iii) The interaction force and the external force are applied to all solid boundary nodes, the total force and the torque acting on the particle are calculated according to Equations (8) and (9), the particle velocity and position are updated by numerical integration, and the particle deformation is calculated by LSM.
(iv) The interaction force also acting back on the fluid lattice nodes is computed by Equation (6) and the fluid field is solved by the modified LBM equation (14). The computations loop back to step (ii).

3. SAMPLE PROBLEMS

In this section, we provide some example problems to validate the LBM–EBF method. In Section 3.1, we simulate the rate of rotation of a circular cylinder in confined shear flow as a function of the rate of shear or Reynolds number (*Re*). The results are compared with the experimental data for two confinement ratios. The problem examines the accuracy of computing the shear stress on the surface of a rotating body at moderate *Re*. In this section, we also demonstrate the small fluctuations in SBB that are eliminated by the EBF method. In Section 3.2, we computationally reproduce Jeffery's solution for rotation of a 3D ellipsoid in shear flow at $Re \ll 1$. Comparison of computational results for sedimentation of a sphere in a confined channel with experiments is presented in Section 3.3, including a note on the effect of grid resolution. Computational simulations of single and multiple deformable particles are presented in Section 4.

3.1. A circular cylinder in simple shear flow

The motion of a neutrally buoyant circular cylinder in simple shear flow has been studied over a wide range of Reynolds numbers. The cylinder is free to rotate with center axis on the centerline of the fluid field. Owing to the wall effect, the non-dimensional rotation speed $\dot{\phi}/G$ depends on the Reynolds number, $Re=Ga^2/\nu$, and the flow confinement ratio $\kappa=H/a$, where G is the shear rate, a is the diameter of the cylinder, and H is the channel height. The LBM method uses a computational domain with 1200×200 lattice nodes. The results are compared at two confinement aspect ratios with the experimental data. The non-dimensional angular rate of rotation with different Reynolds numbers and confinement ratios are compared with the experimental data by Poe and Acrivos [36] at $H/a=11.24$ and Zettner and Yoda [37] with $H/a=4$. The non-dimensional rotation rate will decrease more rapidly with the Reynolds number with larger confinement ratio, as shown in Figure 2.

When $H/a \gg 1$, one can show from Jeffery's [39] solution (set $a=b$ in Equation (22)) that in the limit $Re\to 0$, the rate of angular rotation, $\dot{\phi}=G/2$. For the case $H/a=11.4$, the influence of the boundary walls on the circular cylinder is small and therefore $\dot{\phi}/G$

DOI: 10.1002/fld

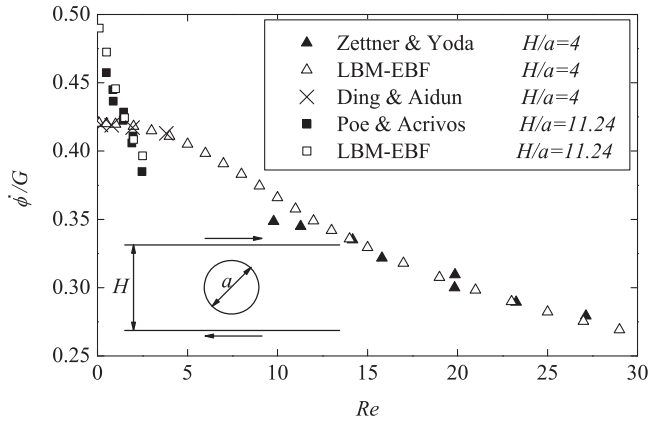

Figure 2. Non-dimensional angular rate of rotation of a torque-free cylinder in simple shear flow. The solid squares (■) and triangles (▲) are the experiment data of Poe and Acrivos [36] and Zettner and Yoda [37], the open squares (□) and open triangles (△) are the results from present LBM with EBF, the crosses (×) are the results from Ding and Aidun [38] with SBB at $Re<5$.

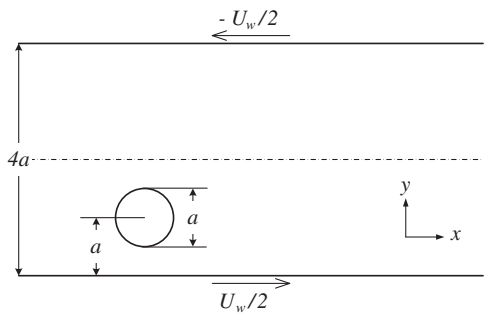

Figure 3. A neutrally buoyant cylinder in simple shear flow, off-center initial position.

approaches ~ 0.5 as $Re \to 0$. For the small confinement ratio, $H/a = 4$, however, the effect of the viscous shear stress on the cylinder due to the presence of the boundary walls becomes significant. The cylinder rotates at a lower angular velocity due to the viscous stress. In the limit of $Re \to 0$, the rotation rate $\dot{\phi}/G \to 0.42$ for $H/a = 4$ is as shown in previous studies [38, 40].

An advantage of the EBF method over SBB is the elimination of small fluctuations, which can be detrimental in the simulation of deformable particles. To demonstrate, consider a cylinder with diameter a positioned at rest half way from the bottom wall to the center between two parallel plates. The plates are $4a$ apart moving in opposite directions with velocity, $U_w/2$, as shown in Figure 3. The computational domain has 2000×80 lattice nodes. The trajectory of the particle toward the centerline computed with LBM with SBB and EBF agrees well, as shown in Figure 4. However, the upward velocity, v, shows fluctuation with SBB as compared with no fluctuation with EBF, as shown in Figure 5. Although the amplitude of the fluctuation in v is small

DOI: 10.1002/fld

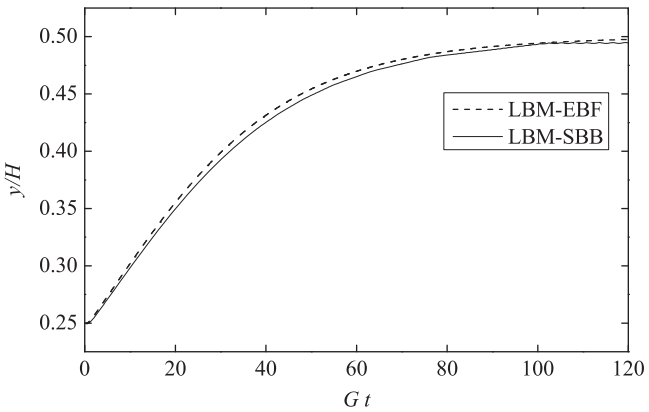

Figure 4. Non-dimensional y position vs non-dimensional time Gt. The solid line is from LBM with SBB and the dash line is from LBM with EBF.

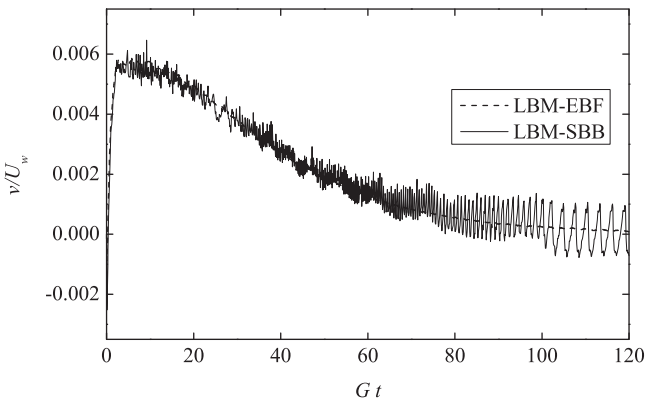

Figure 5. Non-dimensional y direction velocity vs non-dimensional time Gt. The solid line is from LBM with SBB and the dash line is from LBM with EBF.

($\sim$0.2% of U_w), this may result in numerical instability in the application to deformable particles. There is no fluctuation with EBF because the fluid–solid boundary moves continuously across the domain.

3.2. An ellipsoid in simple shear flow

The motion of a solid ellipsoid in a simple shear flow is analyzed in this section. The boundary of this particle is given by

$$\frac{x^2}{a^2}+\frac{y^2}{b^2}+\frac{z^2}{c^2}=1 \tag{20}$$

DOI: 10.1002/fld

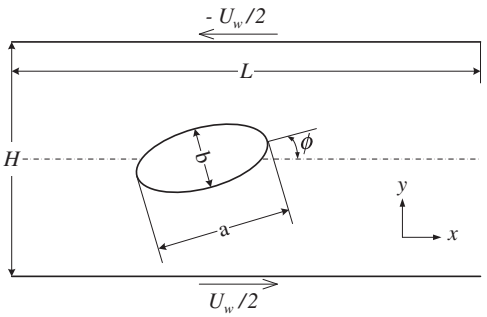

Figure 6. A solid ellipsoid immersed in simple shear flow.

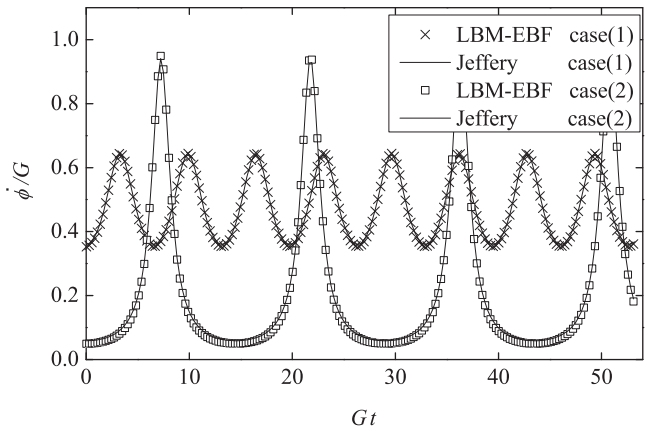

Figure 7. $G=1/6000, a=12, v=1.5, Re=0.064$, Case(1) $b=c=9$, the solid line is Jeffery's solution and the crosses ($\times$) are the simulation result, Case(2) $b=c=3$, the dash line is Jeffery's solution and the open squares ($\square$) are the simulation result.

When one of the principal axes of the ellipsoid is kept parallel to the vorticity vector, as shown in Figure 6, the rotation angle, ϕ, and the angular rate of rotation, $\dot{\phi}$, are given by Jeffery [39]

$$\phi=\tan^{-1}\left(\frac{b}{a}\tan\frac{abGt}{a^2+b^2}\right) \tag{21}$$

$$\dot{\phi}=\frac{G}{a^2+b^2}(b^2\cos^2\phi+a^2\sin^2\phi) \tag{22}$$

where G is the shear rate and t is time. In our simulation, the computational domain is $120\times 120\times 60$ lattice nodes. The Reynolds number $Re=Gd^2/v$, where $d=2a$. For different aspect ratio b/a, the computational results agree very well with Jeffery's analytical solution, as shown in Figure 7. This demonstrates that the no-slip boundary condition on the ellipsoid surface is well satisfied.

DOI: 10.1002/fld

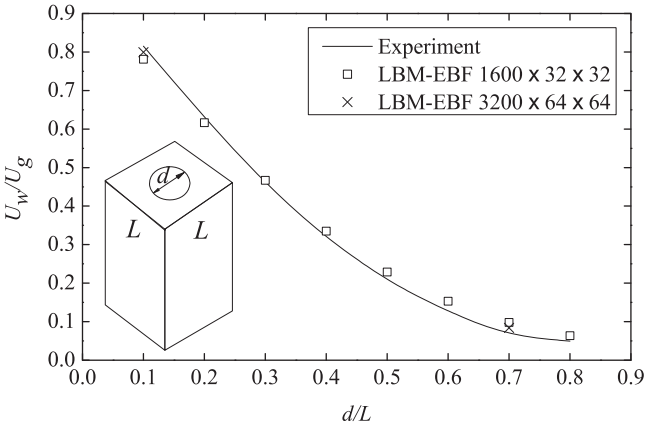

Figure 8. Sedimentation of a sphere in a square cylinder. The curve is the best fit to the experimental data of [41]. The open squares (□) and crosses (×) are the results from LBM–EBF with different grid resolution.

3.3. Sedimentation of a sphere in a square cylinder

A sphere with diameter d is released in a vertical square cylinder of width L settling under gravity force $\mathbf{G}_\mathrm{f}$, as shown in Figure 8. The sphere is initially released at the center of the cross-section of the channel with zero velocity and settles along the axis of the channel reaching a constant velocity. The steady-state settling velocity U_w is normalized with the free settling velocity $U_g = \mathbf{G}_\mathrm{f}/(3\pi\mu d)$ from the Stokes equation.

The simulation results are compared with the experiments of Miyamura *et al.* [41]. In the present analysis, the channel is divided into $1600 \times 32 \times 32$ lattice units. Zero velocity profile is applied at the inlet and the normal derivative of velocity is set to zero at the downstream boundary. The curve is the best fit to the experimental data. Results from a finer grid $3200 \times 64 \times 64$ are also included at $d/L = 0.1$ and 0.7 for evaluating the effect of grid resolution. Figure 8 shows the comparison between the experimental and our computational results.

4. CAPSULES WITH DEFORMABLE MEMBRANE AS A MODEL OF RED BLOOD CELL

In this section, several problems are presented to demonstrate the effects of EBF method. We combine LBM and LSM to simulate the deformable particles in suspension. Deformable particles in the shape of red blood cells are used as an example. It is well known that red blood cell (RBC) deformation is one of the most important aspects of blood rheology. Changes in RBC deformation are known to alter blood flow viscosity [42, 43] and diffusivity [44]. The LBM with EBF presented here is capable of simulating suspensions of RBC at the physiological volume fraction of 47%.

In this paper, a capsule with deformable membrane that has the same geometry and the material properties of real RBC is used. RBC has a complicated membrane structure with a cytoskeleton and phospholipid membrane encapsulating a fluid solution of hemoglobin. Under normal static condition, it has 3D biconcave elastic membranes with elastic shear modulus of 6.6×10^3 dynes/cm [45]. The plasma surrounding the RBC has a viscosity of 1.2 cP at 37°C. The RBC has a major diameter

DOI: 10.1002/fld

of 7.8 μm and a thickness of 2.2 μm at the flank and 0.9 μm at the dimple. These values are used in the following simulation.

4.1. RBC in capillary pressure-driven flow

It is well known from the past experiments that the RBC shape changes into a parachute shape in capillary pressure-driven flow, as shown in Figure 9, retain their shape through the capillary tube, and recover to its original shape in the post capillary region. This unique deformation of the RBC is necessary in nature for high fluidity in micro vessels and for high efficiency of oxygen diffusion to tissue by increasing the surface area and interaction with the endothelial cells.

Several investigators have used this phenomenon to measure the RBC's deformability. In the recent experimental setup of Tsukada *et al.* [46], they use a set of transparent crystal micro channels and a high-speed video camera to capture high-resolution pictures and achieve quantitative data. Dilute suspensions of RBCs passed through a glass capillary tube with a diameter of 9.3 μm were imaged and analyzed. The velocity and the deformation index $\mathrm{DI_P}$ of RBC depend on the pressure gradient in the channel. In this experiment [46], $\mathrm{DI_P}$ is given by

$$\mathrm{DI_P} = \frac{c}{d} \tag{23}$$

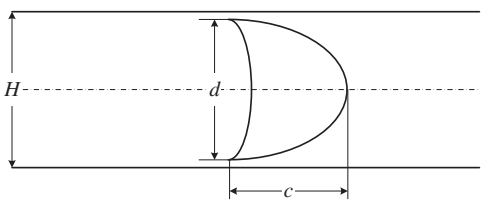

Figure 9. Axisymmetrically deformed RBC in a 'parachute configuration'.

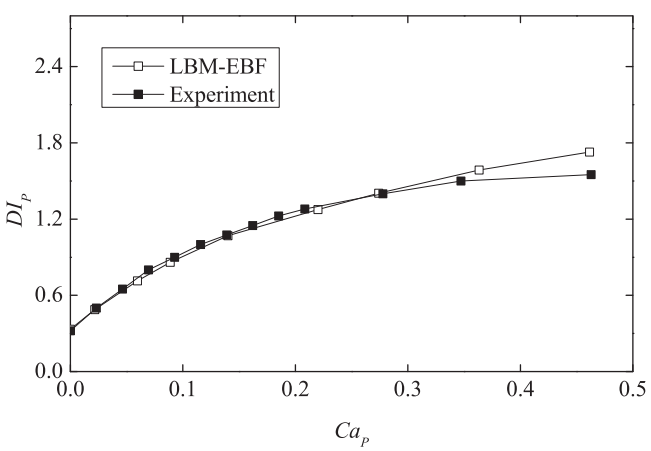

Figure 10. Deformation index $\mathrm{DI_P}$ vs the capillary number Ca_P, the solid squares (■) are the experiment data from Tsukada *et al.* [46] and the open squares (□) are LBM–EBF simulation results.

DOI: 10.1002/fld

Here, d is the diameter of the deformed RBC in the parachute configuration and c is the length of RBC along the axial direction as shown in Figure 9. The simulation results are compared with the experimental results [46]. The Capillary number Ca_P in Figure 10 is defined as

$$Ca_P = \frac{\mu U_x}{S} \tag{24}$$

where μ is the viscosity of the suspending fluid, U_x is the RBC velocity and S is the membrane shear modulus.

The RBC deformation index DI_P is shown in Figure 10 as a function of Capillary number Ca_P. The simulations agree well with experiments up to $Ca_P \approx 0.35$ where we see a deviation between the results.

4.2. Bulk viscosity of blood

The non-Newtonian shear-thinning viscosity of blood is well documented [47, 48] with RBC deformation recognized as one of the most important factors in suspension viscosity [42, 43].

At a high volume fraction, blood is often described by Casson's model, given by

$$\sqrt{\tau_{\text{eff}}} = \sqrt{\tau_{\text{yield}}} + C\sqrt{G} \tag{25}$$

where τ_{eff} is the effective suspension shear stress, τ_{yield} is the yield stress of the suspension in shear, C is a constant and G is the shear rate. The reduced viscosity of blood is defined as

$$\mu_r = \frac{\mu_{\text{eff}}}{\mu} \tag{26}$$

where $\mu_{\text{eff}} = \tau_{\text{eff}}/G$ is the effective suspension viscosity, μ is the viscosity of the suspending fluid. A Casson fluid exhibits non-Newtonian and shear-thinning behavior. The reduced viscosity μ_r is a function of shear Capillary number Ca_{s}, which is defined as

$$Ca_{\text{s}} = \frac{\mu G R}{S} \tag{27}$$

where G is the shear rate and R is the average undeformed RBC cross-section radius when viewed from the side. Here the shear rate $G = U_w/H$, where U_w is the velocity difference between the top and bottom walls, H is the channel height.

The reduced viscosity can be successfully simulated with $O(10^2)$ particles [9, 49]. To study the blood rheology at continuum-level scales, 120 RBCs are simulated at 47% volume fraction with $0.0149 < Ca_{\text{s}} < 0.1342$, corresponding to shear rate ranging between 16 and $144\,\text{s}^{-1}$, respectively. The plasma has a viscosity of 1.58 cP with a density of $1030\,\text{kg/m}^3$ at 25°C [45, 50]. Simulations of 80, 120, and 160 RBCs produce the same result in bulk viscosity. The cases with $Ca_{\text{s}} < 0.01$ are not compared here due to the influence of non-hydrodynamic particle interactions that lead to RBC aggregates known as rouleaux [51]. It is shown in Figure 11 that the simulation results have a similar profile close to the experimental data reported by Brooks *et al.* [47]. The snapshot of a layer of RBCs is shown in Figure 12 to show the strong interaction and deformation of the particles.

DOI: 10.1002/fld

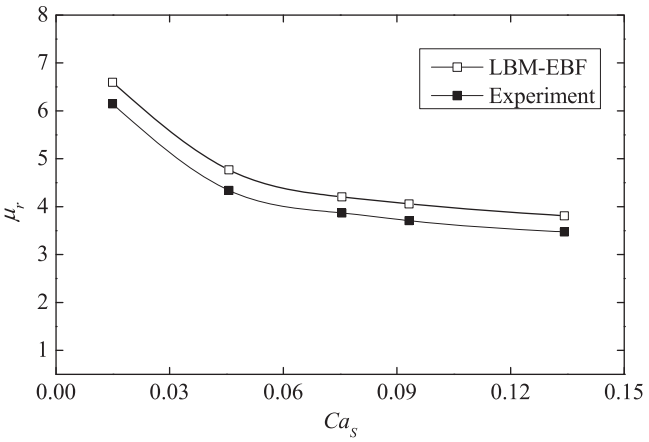

Figure 11. The open squares (□) are the reduced suspension viscosity of simulations of 120 RBCs at 47% volume fraction as a function of Ca_s. The solid squares (■) are the experimental data reported by Brooks *et al.* [47] at 25°C with 47.6% volume fraction.

Figure 12. Example simulation of 120 RBCs at 46.7% volume fraction.

DOI: 10.1002/fld

5. CONCLUSIONS

We have presented the LBM with external boundary force (EBF) method for fluid–solid interaction problems. The novel application to the lattice Boltzmann method (LBM) provides an efficient and more stable computational tool compared with the conventional LBM with SBB, particularly for large number of deformable particles suspended in viscous flow. By coupling with LSM, one can easily re-mesh the solid for different geometries. We can also prescribe the motion of the deformable particle. The operations in LBM with EBF are local, it can be easily programmed for parallel machines. The method has been validated by comparing the 3D computational results with the experimental results and theoretical solutions. With this method, deformable particles may have different densities than the fluid and each particle can have different elastic properties with no additional demand on computational time.

REFERENCES

1. Chen H, Chen S, Matthaeus WH. Recovery of the Navier–Stokes equations using a lattice-gas Boltzmann method. *Physical Review A* 1992; **45**:5339.
2. Hou S, Zou Q, Chen S, Doolen G, Cogley AC. Simulation of cavity flow by lattice Boltzmann method. *Journal of Computational Physics* 1995; **118**:329.
3. Mcnamara GR, Zanetti G. Use of the Boltzmann equation to simulate lattice-gas automata. *Physical Review Letters* 1988; **61**:2332.
4. Aidun CK, Lu Y. Lattice-Boltzmann simulation of solid particles suspended in fluid. *Journal of Statistical Physics* 1995; **81**:49–61.
5. Aidun CK, Lu Y, Ding E. Direct analysis of particulate suspensions with inertia using the discrete Boltzmann equation. *Journal of Fluid Mechanics* 1998; **373**:287.
6. Ladd AJC. Numerical simulations of particulate suspensions via a discretized Boltzmann equation. Part 1. Theoretical foundation. *Journal of Fluid Mechanics* 1994; **271**:285.
7. Buxton GA, Verberg R, Jasnow D, Balazs AC. Newtonian fluid meets an elastic solid: coupling lattice Boltzmann and lattice–spring models. *Physical Review E* 2005; **71**:056707.
8. Dupin M, Halliday I, Care C, Alboul L, Munn L. Modeling the flow of dense suspensions of deformable particles in three dimensions. *Physical Review E* 2007; **75**:066707.
9. MacMeccan RM, Clausen JR, Neitzel GP, Aidun CK. Simulating deformable particle suspensions using a coupled lattice-Boltzmann and finite-element method. *Journal of Fluid Mechanics* 2009; **618**:13.
10. Bouzidi M, Firdaouss M, Lallemand P. Momentum transfer of a Boltzmann-lattice fluid with boundaries. *Physics of Fluids* 2001; **13**:3452.
11. Ginzburg I, d'Humieres D. Multireflection boundary conditions for lattice Boltzmann models. *Physical Review E* 2003; **68**:066614.
12. Yu D, Mei R, Luo L, Shyy W. Viscous flow computations with the method of lattice Boltzmann equation. *Progress in Aerospace Sciences* 2003; **39**:329.
13. Chun B, Ladd AJC. Interpolated boundary condition for lattice Boltzmann simulations of flows in narrow gaps. *Physical Review E* 2007; **75**:066705.
14. Ding E, Aidun CK. Extension of the lattice-Boltzmann method for direct simulation of suspended particles near contact. *Journal of Statistical Physics* 2003; **112**:685.
15. Holdych DJ. Lattice Boltzmann method for diffuse and mobile interfaces. *Ph.D. Thesis*, University of Illinois at Urbana Champaign, 2003.
16. Noble DR, Torczynski JR. A lattice Boltzmann method for partially saturated computational cells. *International Journal of Modern Physics C* 1998; **9**:1189–1201.
17. Strack O, Cook B. Three-dimensional immersed boundary conditions for moving solids in the lattice-Boltzmann method. *International Journal for Numerical Methods in Fluids* 2007; **55**:103.
18. Peskin CS. Numerical analysis of blood flow in the heart. *Journal of Computational Physics* 1977; **25**:220–252.
19. Feng Z, Michaelides E. The immersed boundary-lattice Boltzmann method for solving fluid–particles interaction problems. *Journal of Computational Physics* 2004; **195**:602.

DOI: 10.1002/fld

20. Zhang J, Johnson P, Popel A. An immersed boundary lattice Boltzmann approach to simulate deformable liquid capsules and its application to microscopic blood flows. *Physical Biology* 2007; **4**:285.
21. Goldstein D, Handler R, Sirovich L. Modeling a no-slip flow boundary with an external force field. *Journal of Computational Physics* 1993; **105**:354–366.
22. Buxton GA, Care CM, Cleaver DJ. A lattice spring model of heterogeneous materials with plasticity. *Modelling and Simulation in Materials Science and Engineering* 2001; **9**:485–497.
23. Liboff R. *Kinetic Theory*: *Classical*, *Quantum*, *and Relativistic Descriptions* (3rd edn). Springer: Berlin, 2003.
24. Buick JM, Greated CA. Gravity in a lattice Boltzmann model. *Physical Review E* 2000; **61**:5307.
25. Guo Z, Zheng C, Shi B. Discrete lattice effects on the forcing term in the lattice Boltzmann method. *Physical Review E* 2002; **65**:046308.
26. He X, Zou Q, Luo LS, Dembo M. Analytic solutions and analysis on non-slip boundary condition for the lattice Boltzmann BGK model. *Journal of Statistical Physics* 1997; **87**:115.
27. Ladd AJC, Verberg R. Lattice-Boltzmann simulation of particle–fluid suspensions. *Journal of Statistical Physics* 2001; **104**:1191.
28. Martys NS, Shan X, Chen H. Evaluation of the external force term in the discrete Boltzmann equation. *Physical Review E* 1998; **58**:6855.
29. Peskin CS. The immersed boundary method. *Acta Numerica* 2002; **11**:479.
30. Chapman S. On the law of distribution of molecular velocities, and on the theory of viscosity and thermal conduction, in a non-uniform simple monatomic gas. *Philosophical Transactions of the Royal Society* 1916; **216**:279–348.
31. Enskog D. Kinetische theorie der vorgaenge in maessig verduennten G. *Ph.D. Thesis*, Uppsala, 1917.
32. Ginzburg I, d'Humieres D. Principles of the kinetic theory of gases. *Handbuch der Physik* 1958; **12**:205.
33. Arbabi S, Sahimi M. Test of universality for three-dimensional models of mechanical breakdown in disordered solids. *Physical Review B* 1990; **41**:772.
34. Schwartz LM, Feng S, Thorpe MF, Sen PN. Behavior of depleted elastic networks: comparison of effective-medium and numerical calculations. *Physical Review B* 1985; **32**:4607.
35. Alexeev A, Verberg R, Balazs AC. Modeling the motion of microcapsules on compliant polymeric surfaces. *Macromolecules* 2005; **38**:10244.
36. Poe GG, Acrivos A. Closed-streamline flows past rotating single cylinders and spheres: inertia effects. *Journal of Fluid Mechanics* 1975; **72**:605.
37. Zettner CM, Yoda M. The circular cylinder in simple shear at moderate Reynolds numbers: an experimental study. *Experiments in Fluids* 2001; **30**:346.
38. Ding E, Aidun CK. The dynamics and scaling law for particles suspended in shear flow with inertia. *Journal of Fluid Mechanics* 2000; **423**:317.
39. Jeffery GB. The motion of ellipsoidal particles immersed in a viscous fluid. *Proceedings of the Royal Society of London*, *Series A* 1922; **102**:161.
40. Mikulencak DR, Morris JF. Stationary shear flow around fixed and free bodies at finite Reynolds number. *Journal of Fluid Mechanics* 2004; **520**:215.
41. Miyamura A, Iwasaki S, Ishii T. Experimental wall correction factors of single solid spheres in triangular and square cylinders, and parallel plates. *International Journal of Multiphase Flow* 1981; **7**:41.
42. Kim D, Beissinger RL. Augmented mass transport of macromolecules in sheared suspensions to surfaces. *Journal of Colloid and Interface Science* 1993; **159**:9–20.
43. Shin S, Ku Y, Park MS, Suh JS. Measurement of red cell deformability and whole blood viscosity using laser-diffraction slit rheometer. *Korea–Australia Rheology Journal* 2004; **16**:85–90.
44. Cha W, Beissinger RL. Augmented mass transport of macromolecules in sheared suspensions to surfaces b. Bovine serum albumin. *Journal of Colloid and Interface Science* 1996; **178**:1.
45. Waugh R, Evans EA. Thermoelasticity of red blood cell membrane. *Biophysical Journal* 1979; **26**:115.
46. Tsukada K, Sekizuka E, Oshio C. Direct measurement of erythrocyte deformability in diabetes mellitus with transparent microchannel capillary model and high-speed video camera system. *Microvascular Research* 2001; **61**:231–239.
47. Brooks DE, Goodwin JW, Seaman GV. Interactions among erythrocytes under shear. *Journal of Applied Physiology* 1970; **28**:172–177.
48. Merrill EW, Cokelet GC, Britten A, Wells RE. Non-Newtonian rheology of human blood—effect of fibrinogen deduced by 'subtraction'. *Circulation Research* 1963; **13**:48–55.

DOI: 10.1002/fld

49. Sierou A, Brady JF. Rheology and microstructure in concentrated noncolloidal suspensions. *Journal of Rheology* 2002; **46**:1031–1056.
50. Harkness J, Whittington RB. Blood–plasma viscosity: an approximate temperature invariant arising from generalised concepts. *Biorheology* 1970; **6**:169–187.
51. Fung Y. *Biomechanics*: *Mechanical Properties of Living Tissues*. Springer: Berlin, 1993.

DOI: 10.1002/fld